Journal of Materials Science & Nanotechnology
Volume 11 | Issue 1
ISSN: 2348-9812

Research Article Open Access

The Effect of the Morphology Optimization of Precursor with Different Nickel Content on the Performance of Lithium-Ion Battery Cathode Materials

Hailan Feng [1,2,3], Yuxing Xu [1,3], Pei Li [4], Jianlin Feng [4], Yuncheng Zhou [1,2,3], Jiechen Song [1,2,3], Jun Yang [1], Qiangqiang Tan [1,3,*]

[1]State Key Laboratory of Multiphase Complex Systems, Institute of Process Engineering, Chinese Academy of Sciences, Beijing 100190, China

[2]School of Chemical Engineering, University of Chinese Academy of Sciences, Beijing, 100049, China

[3]Hebei Engineering Research Center of Power and Energy Storage Battery Materials, Hebei Technology Innovation Center of Advanced Energy Materials, Hebei Manufacturing Industry Innovation Center of New Energy Materials and Key Equipment, Langfang Technological Service Center of Green Industry, Langfang 065001, China

[4]China Science Maanshan New Materials Science and Technology Innovation Park Co. Ltd, Anhui 243000, China

[*]**Corresponding Author:** Qiangqiang Tan, State Key Laboratory of Multiphase Complex Systems, Institute of Process Engineering, Chinese Academy of Sciences, Beijing 100190, China and Hebei Engineering Research Center of Power and Energy Storage Battery Materials, Hebei Technology Innovation Center of Advanced Energy Materials, Hebei Manufacturing Industry Innovation Center of New Energy Materials and Key Equipment, Langfang Technological Service Center of Green Industry, Langfang 065001, China. Tel: +13910112386, E-mail: qtan@ipe.ac.cn.

Citation: Hailan Feng, Yuxing Xu, Pei Li, Jianlin Feng, Qiangqiang Tan, et al., (2023) The Effect of the Morphology Optimization of Precursor with Different Nickel Content on the Performance of Lithium-Ion Battery Cathode Materials. J Mater Sci Nanotechnol 11(1): 103

Received Date: April 09, 2023 **Accepted Date:** April 10, 2023 **Published Date:** May 09, 2023

Abstract

Increasing the nickel content in the layered $LiNi_xCo_yMn_zO_2$ ($x + y + z = 1$), the most promising cathode materials for lithium ion batteries (LIBs), has been a dominant strategy to increase their energy density. In this study, we report the control on the primary particle morphology of precursors with different nickel contents, e.g. $Ni_{0.5}Co_{0.2}Mn_{0.3}(OH)_2$, $Ni_{0.6}Co_{0.2}Mn_{0.2}(OH)_2$ and $Ni_{0.8}Co_{0.1}Mn_{0.1}(OH)_2$ by adjusting the preparation process. The scanning electron microscopy (SEM) images demonstrate that by decreasing the pH value and increasing the ammonia concentration, the order of precursors with different nickel contents increases, resulting in gradually directional and orderly stack or interlaced arrangement in the primary particles. With the increase of nickel content, the precursor changes from nano-sheet stacking like plug-in stereoscopic spheres to nano-needle interweaving like wool balls, all of which tend to grow in the direction of [001]. The final layered cathode materials that well inherit the precursor morphologies benefit the growth of the [003] crystal axis, predominantly having a good layered structures and low cation mixing degrees and exhibiting superior rate capability and good cycle stability due to faster Li^+ transport. Especially, the ordered high nickel cathode material has a higher Li-ion diffusion rate. With the increase of nickel content, the morphology distribution of the precursor has a more significant effect on

the electrochemical properties of the cathode materials.

Keywords: Cathode materials; Lithium-ion batteries; Energy density; Primary particles; Li-ion diffusion

Introduction

With the ever-growing serious environmental pollution and the energy needs, it is more urgent to develop and find new alternative energy sources. Lithium-ion batteries (LIBs) is widely applied in the fields of 3C (computer, communication, and consumer electronics) products and electric vehicles (EVs) due to their high energy density and long service life [1-4]. In recent years, as the demand for LIBs grows exponentially to feed the nascent electric-vehicle and grid-storage markets, the need for higher energy density and longer cycle life becomes more apparent [5-7]. Among commercial cathode materials, the layered $LiNi_xCo_yMn_zO_2$ (LiNCM, $x + y + z = 1$) is considered to be the most promising positive electrode material, due to its low cost, high capacity and distinguished safety performance. Increasing the nickel content in the layered NCM cathodes has been an effective strategy to boost the energy density of LIBs [8-11].

However, there are still many challenges in the development of NCM cathode materials. Due to the similar radius of Li^+ (0.076 nm) and Ni^{2+} (0.069 nm), the Li^+/ Ni^{2+} ion exchange known as cation mixing would seriously affect the Li^+-ion diffusion, causing drastic structural degradation and poor electrochemical performances [12,13]. On the other hand, the surface side reaction and the dissolution of transition metals will also reduce the electrochemical properties of the materials [14-16]. At the same time, with the increase of nickel content, materials will also face a series of problems, such as easy formation of non-stoichiometric ratio, high total alkali content, poor thermal stability and safety performance [17-19]. In order to resolve the above-mentioned problems, many researchers focus on the surface coating and ion doping [20-25], but rarely emphasize the analysis of the inner structure. Especially, there is no systematic study on the internal structure regularity and influencing factors of NCM with different nickel content.

The typical commercial NCM cathode materials are composed of primary nanoparticles that form spherical secondary particles with size of ca. 10 μm. The interfaces among inner particles inevitably lead to the collapse of the cathode materials during the repetitive lithiation/delithiation process [26-28]. Therefore, the internal arrangement of primary particles has a great influence on the physical and chemical properties of the materials [29,30]. The structural characteristics of the cathode materials inherit the structural features of the precursors [31]. Thus, it is of great significance to fundamentally understand the inner structures of the precursors on the electrochemical performance of the cathode materials.

In this paper, we would systematically investigate the morphology controlling of three kinds of agglomerated precursors with different nickel contents. According to the testing results, all different nickel content precursors gradually are well-directional along the [001] plane. The difference is that with the increase of pH conditions of high nickel precursor, the primary particles are gradually transformed from self-assembly of nanosheets to nanoneedles. The positive electrode material inherits the structural orientation characteristics of the precursor, and the highly ordered samples have high solid density and crystallinity. When the degree of ordered grain orientation increases, the electrochemical performances can be dramatically improved. The electrochemical impedance results show that the cathode materials with plug-in stacking and interleaveing structures have a low Li^+ diffusion barrier, and can inhibit the surface and interface side reactions, thus improving the electrochemical performance of the materials. With the increase of the nickel content, the impact of the precursor structure on the electrochemical performance of the positive electrode material is more significant.

Experimental Section

Synthesis of Precursor and Cathode Materials

The spherical precursors, i.e., $Ni_{0.5}Co_{0.2}Mn_{0.3}(OH)_2$, $Ni_{0.6}Co_{0.2}Mn_{0.2}(OH)_2$ and $Ni_{0.8}Co_{0.1}Mn_{0.1}(OH)_2$ (labeled as PN5, PN6, PN8, respectively) were prepared by coprecipitation method. The $NiSO_4 \cdot 6H_2O$, $CoSO_4 \cdot 7H_2O$ and $MnSO_4 \cdot H_2O$ with molar ratios of 5:2:3, 6:2:2 and 8:1:1, respectively, were simultaneously dissolved in deionized water to form 2.0 mol L^{-1} mixed metal salt solutions. A stoichiometric amount of NaOH solution (used as a precipitating agent) and $NH_3 \cdot H_2O$ solution (as a chelating agent) were separately pumped into the above solutions at the same time under the atmosphere of argon, and the reaction was carried out in a water bath at 55 ^{0}C The PN5 precursors (labeled as PN5-1, PN5-2 and PN5-3) were synthesized by regulating the pH values as 11.0, 10.8, 10.6, and by adding 0.4, 0.8, and 1.2 mol L^{-1} ammonia solutions, respectively. The pH values of PN6 precursors (labeled as PN6-1, PN6-2 and PN6-3) were kept at 11.4, 11.2, 11.0 with the concentrations of ammonia solutions of 1.0, 1.5, and 2.0 mol L^{-1}, while the pH values of PN8 precursors (labeled as PN8-1, PN8-2 and PN8-3) were kept at 12.2, 12.0, 11.8, with the concentration of ammonia solutions of 2.5, 3.0, and 3.5 mol L^{-1}, respectively. All the obtained precursors were filtered and washed with deionized water and then dried in a vacuum oven at 120 ^{0}C for 6 h. The dried precursors were then milled with 5% excess of Li_2CO_3 or LiOH for 4 h, followed by heating at 95 ^{0}C, 870 ^{0}C, 750 ^{0}C in air or oxygen for 10 h, the cathode materials were labeled CN5-1, CN5-2, CN5-3, CN6-1, CN6-2, CN6-3, CN8-1, CN8-2 and CN8-3, respectively.

Materials Characterization

The particle size distribution was measured on a laser diffraction instrument (Dandong stersizer 2000). The BET (Brunauer–Emmett–Teller method) specific surface areas were evaluated by N_2 adsorption and desorption isothermals (Kubo-1200). The tap density was measured by FT-100E powder density instrument. The crystalline structures were examined by X-ray diffraction (XRD, Shimadzu 7000S/L), where the angel 2θ was scanned over 10°-80° and the step size was 2^0 min^{-1}. The morphologies of the samples were characterized using a scanning electron microscope (SEM, Hitachi S-4800). The transmission electron microscopy (TEM) and the high-resolution TEM (HRTEM) characterizations were carried out on a FEI Tecnai F20 instrument.

Electrochemical Tests

To test the electrochemical property of the electrode materials, the active material, acetylene black and polyvinylidene difluoride were distributed in N-methyl pyrrolidinone (with a mass ration of 92:5:3) and stirred vigorously to obtain the electrode slurry. The slurry was then casted on aluminum foil, followed by drying at 120 ^{0}C for 24 h in vacuum oven. The prepared cathode electrodes were punched to form the disks (ø = 14 mm), and the electrode pressed density was about 2.6 g cm^{-3}. Cathode materials, lithium metal foil, Celgard 2400 porous polypropylene film and electrolyte of $LiPF_6$ (1 mol L^{-1}) dissolved in a mixture of EC/DMC/EMC (1:1:1 by volume) were included in the CR2025 coin-type cells, which were packaged in a pure Argon-filled glovebox. The cells were assembled in an argon-filled glove box with H_2O and O_2 concentrations below 0.01 ppm. All the electrochemical performances were performed on a Xinwei CT2001C (shenzheng, China) battery program-control test system between 3.0 and 4.3 V at different charge/discharge rate at 25 ^{0}C. CV was conducted between 3.0 and 4.3 V at the scanning speed of 0.1 mV s^{-1}.The electrochemical impedance spectroscopy (EIS) of the recirculating material was measured at an amplitude of 5 mv in the frequency range of 10^5-10^{-2} Hz (CHI660E, Shanghai, China). The EIS measurements were performed after 100 cycles (1 C/1 C).

Results and Discussion

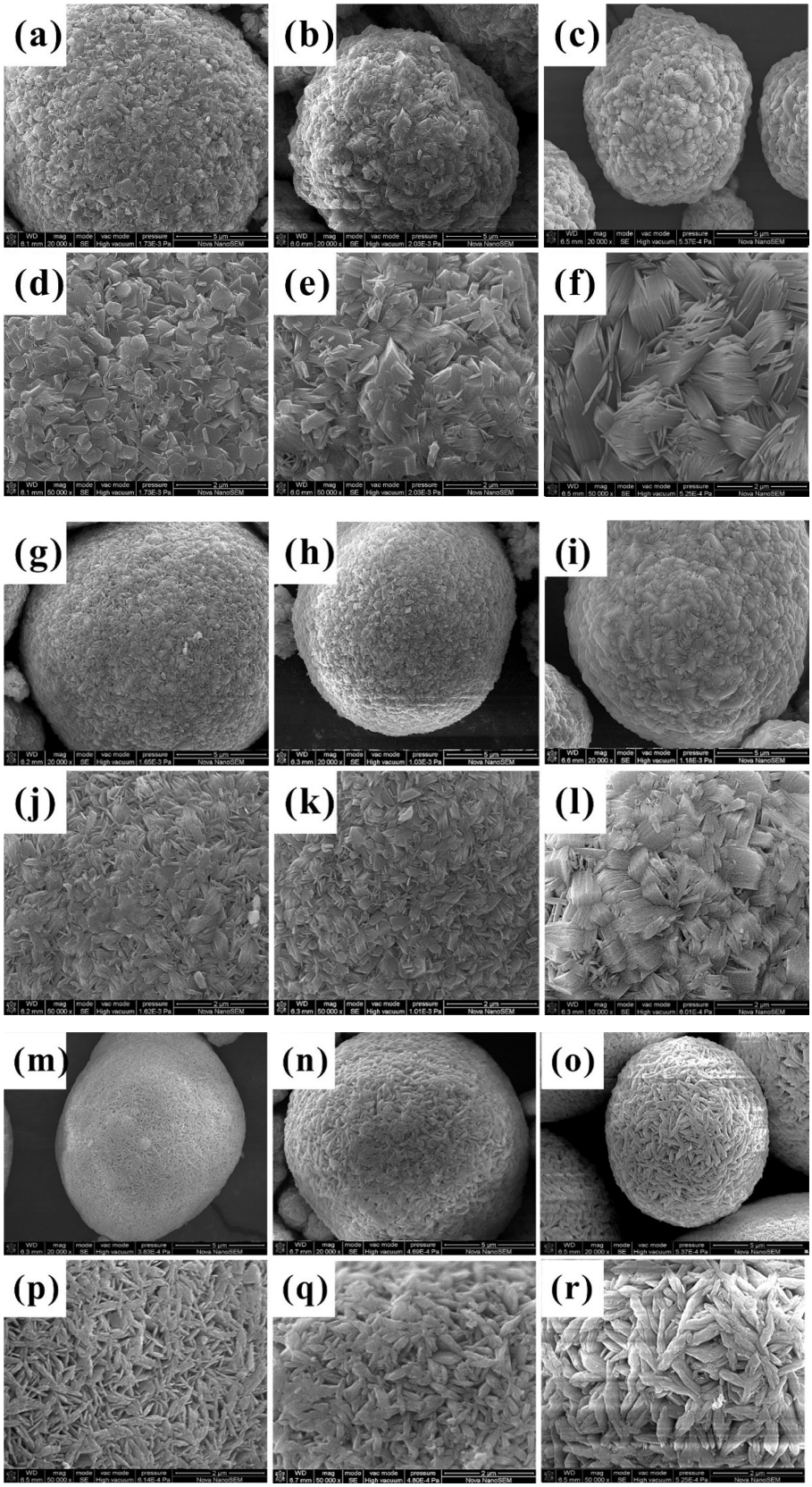

Figure 1: SEM images of (a,d) PN5-1, (b,e) PN5-2, (c,f) PN5-3, (g,j) PN6-1, (h,k) PN6-2, (i.l) PN6-3, (m,p) PN8-1, (n,q) PN8-2, and (o,r) PN8-3.

SEM was used to observe the morphologies of three different hydroxide agglomerating precursors and their final cathode materials. As indicated in Figure 1, all precursors exhibit obvious secondary particles of 10–12 μm, which are aggregated by primary

nano-particles. However, obvious differences could be discerned in the morphology and assembly method of primary particles. In Figure 1a-f, the PN5-1 precursors comprise of nanosheets with a disordered state of attachment, while the PN5-2 precursors show the coexistence of adhesion and intercalation. Obviously, the primary particles of PN5-3 are stacked into intercalated layers to form plug-in stereoscopic sphere. The pH values and the concentration of $NH_3 \cdot H_2O$ turn out to be the critical factors in determining the size and the directional growth of primary particles [32-35]. The change regulation of morphology of PN6 precursors is similar to that of PN5, as shown in Figure 1g–l, but the thickness of the assemblies formed by primary nanosheets is thinner than that of PN5. Compared with PN-5 and PN-6, the pH value of PN-8 reaction system is higher, so the morphology of primary particle is significantly different (denoted as nanoneedles), but the trend of grain growth arrangement is the same. As seen from the Figure 1m–r, the PN8-1 shows that it has uneven growth, and the PN8-2 is semi-ordered and the PN8-3 is ordered like interweaving wool balls.

Figure 2 clearly shows the schematic diagram of hydroxide precursors with different nickel content prepared under different reaction conditions. In general, with the increase of nickel content, the precursor changes from nano-sheets assembling like plug-in stereoscopic spheres to nano-needles interweaving like wool balls. By regulating the pH values and ammonia concentrations, the ordered degree gradually increases, making the primary particles gradually directional and orderly arranged.

Figure 3 reveals the morphology of the three cathodes, i.e. CN5, CN6 and CN8, showing that the morphology and characteristics inherit their precursors. Table1 shows that the thickness of the CN5 materials increases gradually from 650 nm to 790 nm and 1200 nm, depending on the stacking degree of the nanosheet precursors. Compared with CN5 and CN6, the primary particle size of CN8 is smaller (ca. 460 nm). The reason may be that the primary particles are narrow, and loosely stacked on the surfaces they attached, which would inhibit the crystal growth by affecting the Li^+ transport rate in sintering. Therefore, the morphology and assembly mode of the precursor with different nickel content have great influence on the final cathode morphology.

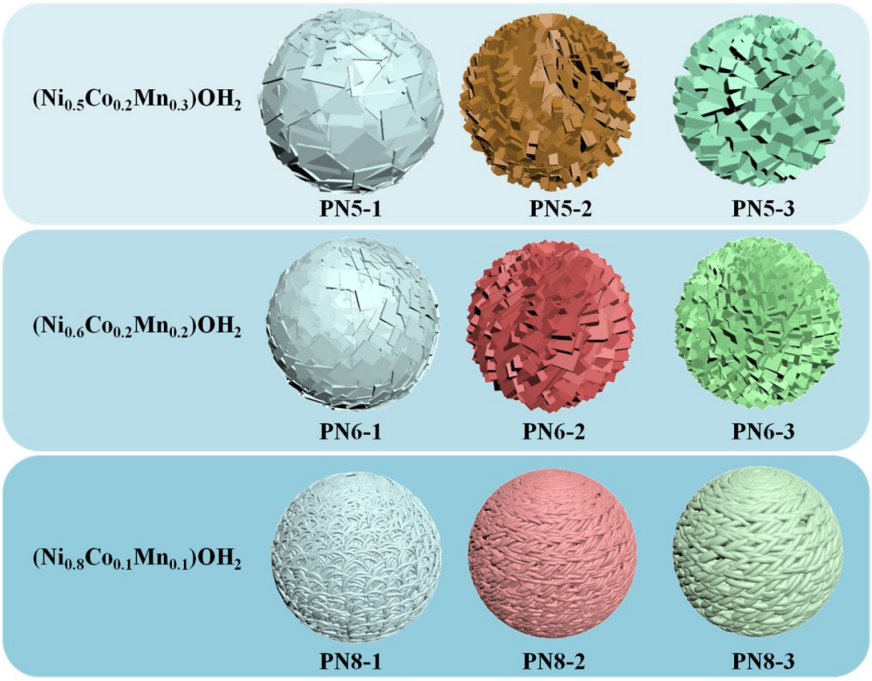

Figure 2: Schematic illustration of three different internal structure of precursors with different nickel content.

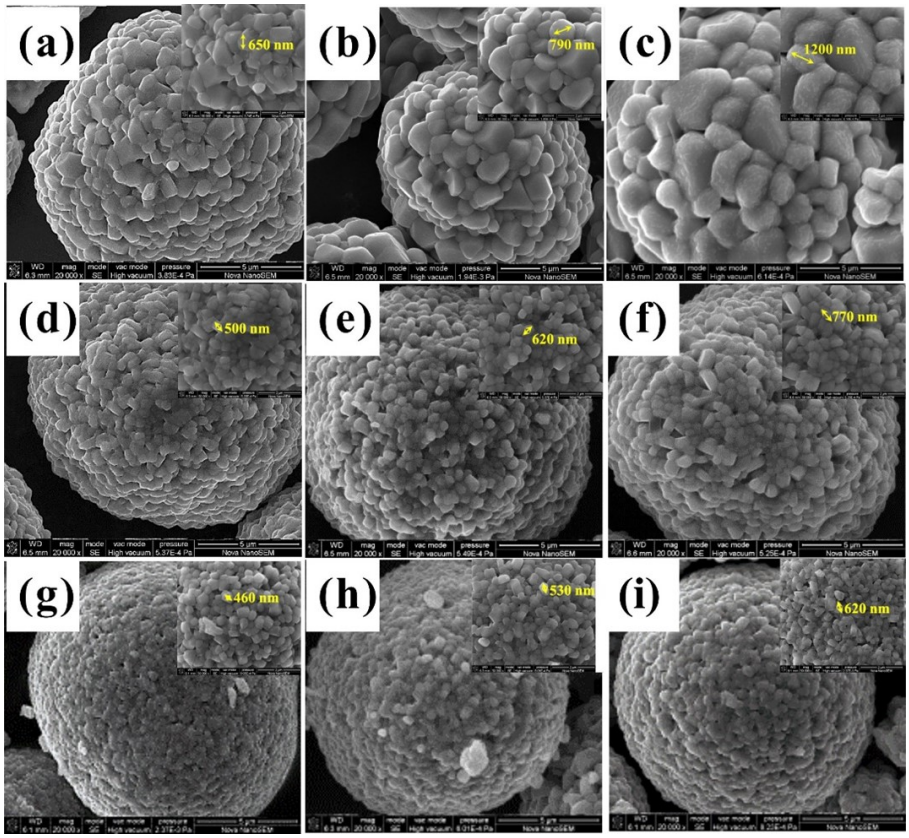

Figure 3: SEM images of (a) CN5-1, (b) CN5-2, (c) CN5-3, (d) CN6-1, (e) CN6-2, (f) CN6-3, (g) CN8-1, (h) CN8-2, and (i) CN8-3.

Table 1: Primary particle size of all prepared cathode materials

Samples	1	2	3
CN5	650 nm	790 nm	1200 nm
CN6	500 nm	620 nm	770 nm
CN8	460 nm	530 nm	620 nm

The TEM and HRTEM with the fast Fourier transform (FFT) graphs were applied to analyze the microstructure of the directional ordered cathodes and precursors. As show in the Figure 4df, the precursors PN5-3, PN6-3 and PN8-3 all show 0.463 nm of typical lattice fringes, corresponding to the (001) plane of the hydroxide compound [26], which indicate that different nickel content crystals prefer orientation of (001) crystal axis at appropriate pH value and ammonia concentration. Meanwhile, the (001) plane is also confirmed in the FFT image. The TEM images of CN5, CN6 and CN8 in Figure 4df display obvious crystal particles. The HRTEM images acquired from the selected areas are showed in Figure 4jl. As observed, all samples have distinct lattice fringes, indicating that a layered structure is formed. The lattice fringes of cathode materials display an interplanar spacing of 0.47 nm, which is consistent with the (003) plane of the layered structure [36]. Meanwhile, the (003) plane is also confirmed in the FFT image. It is reported that this area is part of the {010} active planes [37], which can accelerate the Li-ion transportation and improve the electrochemical properties of cathode materials [38]. Such a growth preference in the final cathode materials can be well inherited from the unique morphology of the precursors with different nickel content.

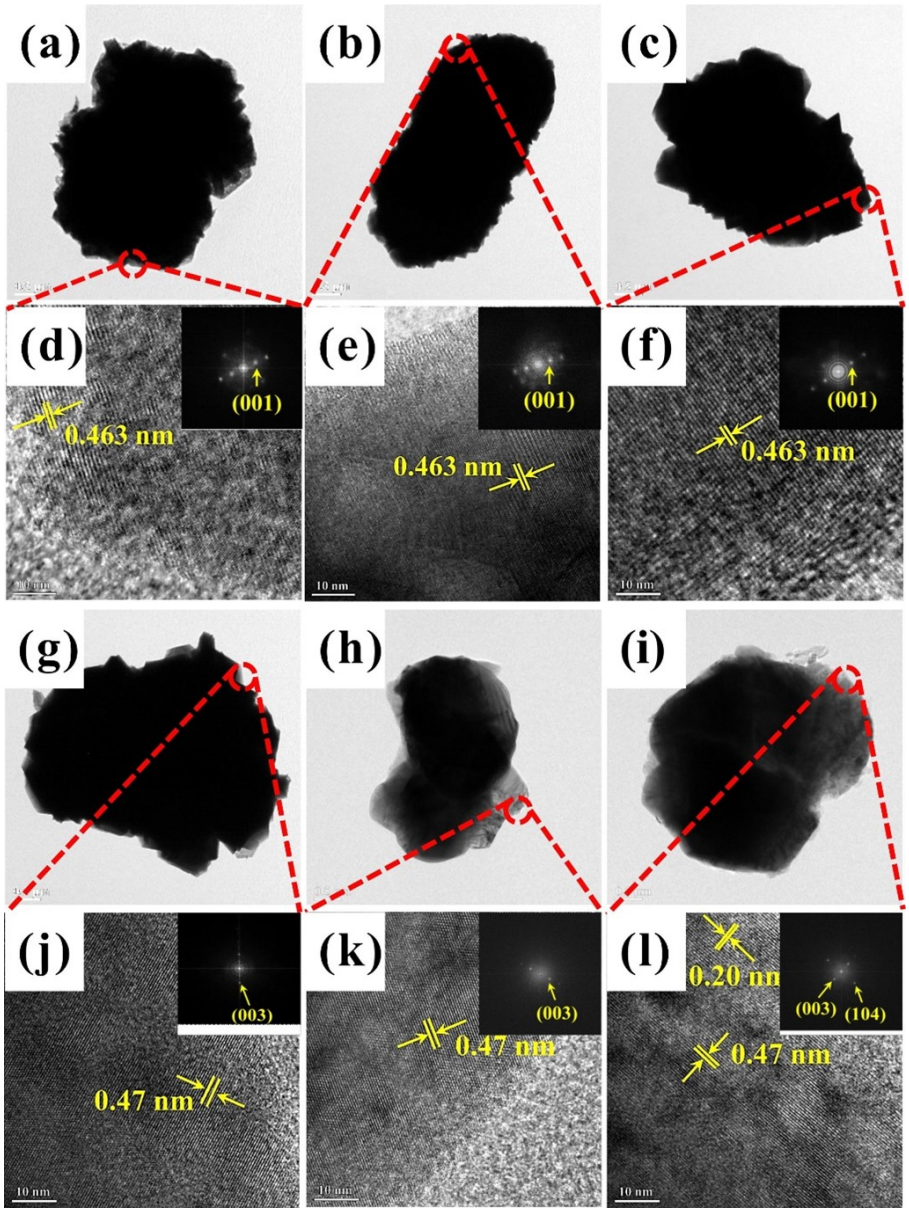

Figure 4: TEM images of the well-orientated precursors (a)PN5-3, (b)PN6-3, (c)PN8-3, (g) CN5-3, (h) CN6-3 and (i) CN8-3; HRTEM images of the (d) PN5-3, (e) PN6-3, (f) PN8-3, (j) CN5-3, (k) CN6-3, (l) CN8-3; and the inset image is the FFT.

The physical properties of the material were further analyzed. It can be seen from Table 2, the well-orientated PN5-3, PN6-3 and PN8-3 have the highest tab density and the lowest specific surface area, indicating that their internal structures are relatively compact, which contribute to the high reactivity for the following solid-state reaction. The trends of tab density and specific surface area of the three nickel-containing cathode materials are highly consistent with precursors. The low tab density will affect the energy density of the materials, while the high specific surface area will cause the side reaction and affect the performance of the materials [39-41].

Table 2: D50, tap density and surface residual alkali of all samples

Materials	D50 (μm)	TD (g/cm^3)	BET (m^2/g)
PN5-1	11.42	2.17	6.8354
PN5-2	11.65	2.25	5.6281
PN5-3	11.51	2.32	4.8572
CN5-1	12.26	2.26	0.3868
CN5-2	12.55	2.38	0.2973
CN5-3	12.45	2.40	0.2227
PN6-1	10.28	2.06	5.5428
PN6-2	10.36	2.18	5.1364
PN6-3	10.24	2.27	4.9266
CN6-1	11.22	2.29	0.3208
CN6-2	11.37	2.32	0.3011
CN6-3	11.41	2.37	0.2845
PN8-1	10.12	2.01	6.3879
PN8-2	10.34	2.05	5.9451
PN8-3	10.71	2.07	5.5621
CN8-1	11.10	2.14	0.7189
CN8-2	11.49	2.20	0.6322
CN8-3	11.92	2.27	0.5005

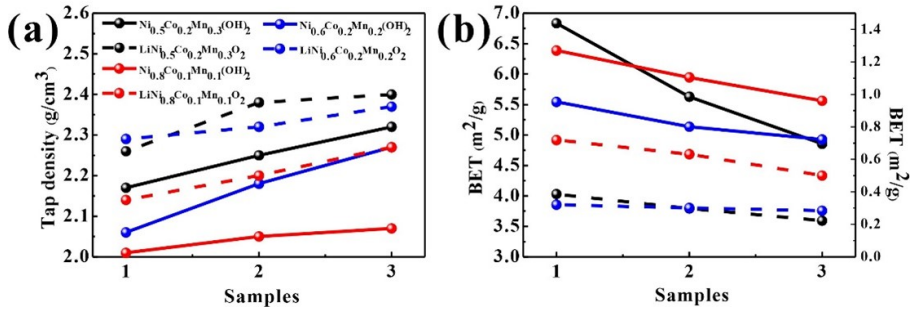

Figure 5: All prepared precursors and corresponding cathode materials (a) Tap density, (b) Specific surface area.

Figure 6 displays the XRD patterns of the precursors and cathode materials. Figure 6a shows that all diffraction peaks of the precursors with the different nickel content can be attributed to the a-$Ni(OH)_2$ structure (P3m1 space group) without any impurities [42-44]. Compared with the disordered precursors, the PN5-3, PN6-3, PN8-3 have well crystallinity. By increasing nickel content of precursors, the [001] peak of the PN8-3 precursor becomes sharp gradually, which is consistent with the TEM results. Figure 6(b,d,f)show the peaks of a typical hexagonal α-$NaFeO_2$ layered structure. In addition, the clear separations of (006)/(012) and (018)/(110) imply the presence of the well-formed layered structure [45-48]. The Rietveld refinement results were summarized in Table 3. The I(003)/I(104) intensity ratio usually reflects the degree of the cation mixing [28]. The I(003)/I(104) values of CN5-3, CN6-3 and CN8-3 are 1.39, 1.32, 1.29, respectively, which are much higher than other disordered cathode materials. In addition the Li^+/ Ni^{2+} mixing degree of CN5-3 is 1.91%, which is smaller than that of CN5-1 (2.61%). This further indicates that the ordered

structure have lower Li^{+}/Ni^{2+} mixed arrangement. The higher nickel cathode material CN8 has a lower I(003)/I(104) than that of CN-5 and CN-6, meaning that crystal particles of the precursor are more conducive to the properties of cathode materials, also as confirmed by the direct evidence provided by HRTEM images. In addition, the increase of orientation leads to higher c/a ratio, which further indicates that the cathode material prepared by ordered intercalated precursor has the best layered structure. Lithium ion diffuses only along a two-dimensional path (as shown in Fig. 6h, so a cathode with an ordered internal structure can provide a fast channel for lithium ion diffusion [49], and could be expected to show an excellent cyclability and rate capability.

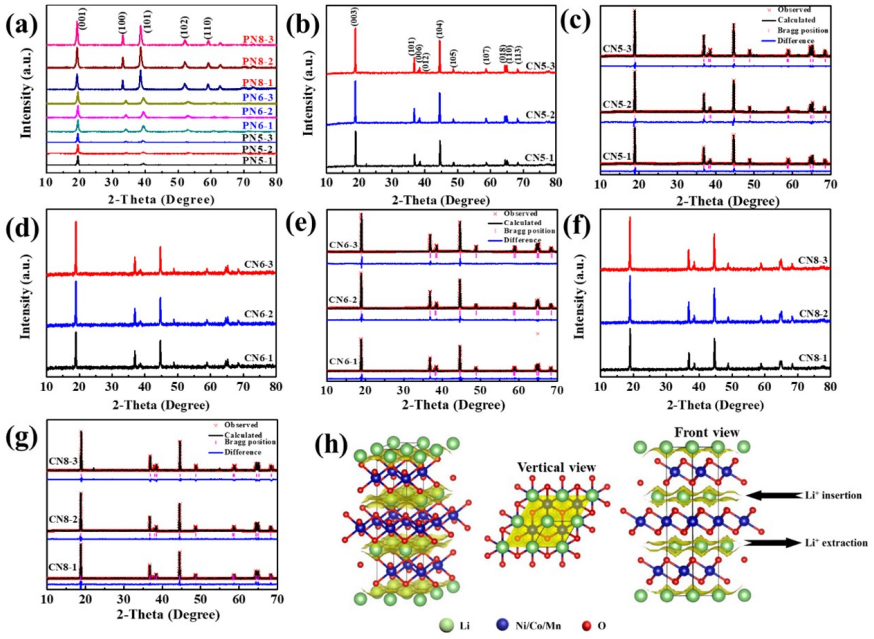

Figure 6: XRD patterns of (a) precursors of PN5, PN6, PN8; XRD patterns of cathode materials of (b) CN5; (d) CN6; (f) CN8; XRD refinement of cathode materials of (c) CN5; (e) CN6; (g) CN8; (h) lithium-ion diffusion channel.

Table 3: Rietveld refinement results of cathode material samples with different crystal structures

Materials	Lattice parameters		c/a	$I_{(003)/(104)}$	Li^{+}/Ni^{2+}	R_{wp}	R_{p}
	a[Å]	c[Å]			mixing(%)		
CN5-1	2.8678	14.0751	4.9080	1.32	2.61%	4.09%	2.57%
CN5-2	2.8698	14.1627	4.9351	1.35	2.26%	5.08%	3.72%
CN5-3	2.8699	14.1636	4.9352	1.39	1.91%	3.60%	3.23%
CN6-1	2.8605	14.0537	4.9131	1.26	2.98%	5.10%	3.98%
CN6-2	2.8617	14.0745	4.9182	1.28	2.52%	4.47%	3.73%
CN6-3	2.8599	14.0726	4.9207	1.32	2.11%	4.29%	2.75%
CN8-1	2.8548	14.0157	4.9095	1.22	4.70%	4.12%	2.49%
CN8-2	2.8549	14.0454	4.9198	1.26	3.93%	5.21%	3.08%
CN8-3	2.8549	14.0469	4.9203	1.29	3.12%	3.95%	2.99%

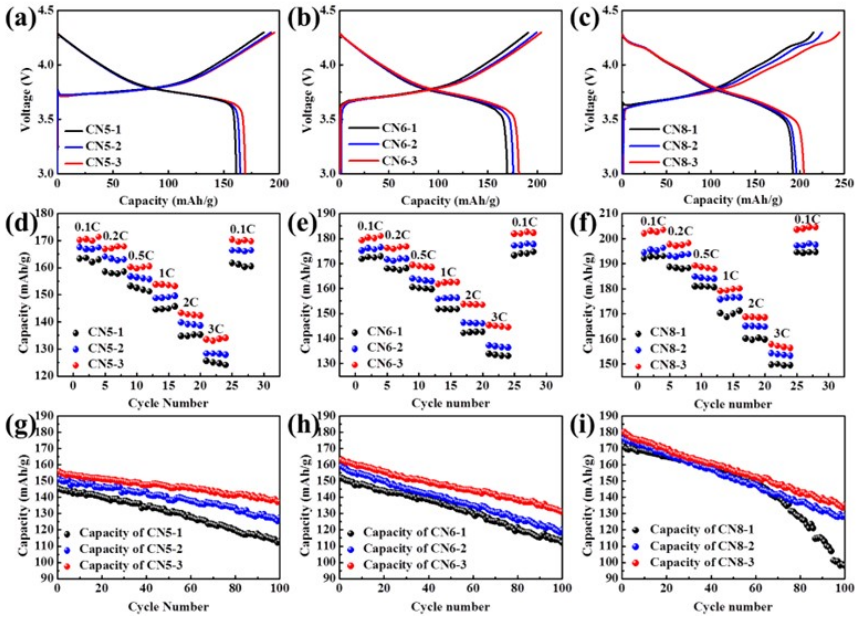

Figure 7: Electrochemical performances (a) first charge and discharge curve; (b) rate performance graph under different discharge rates; (c) cycle performance graph.

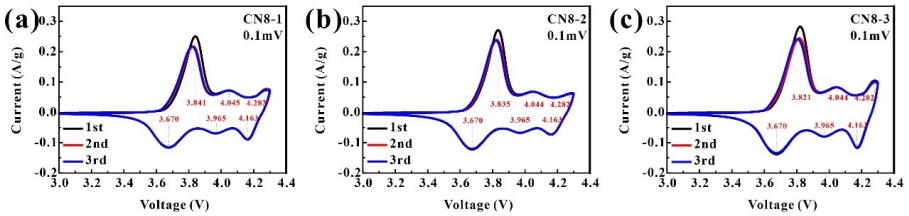

Figure 8: Initial three CV curves at scanning rate of 0.1 mV s^{-1} of (a) CN8-1; (b) CN8-2; (c)CN8-3

The electrochemical property of cathode materials with different nickel content samples are characterized and exhibited in Figure 7. Figure 7ac depict the profile of charge and discharge at 0.1 C between 3.0 and 4.3 V. All samples show typical characteristic curves of layered cathode materials [50-52], It is worth noting that a new platform has appeared in NCM811 materials near 4.2V, which is due to the structural phase transition [43, 47]. Figures 8a-c show the CV profiles of CN8-1, CN8-2 and CN8-3 samples respectively. There present three similar pairs of redox peaks referring to phase transformation of H1-M, M-H2, H2-H3 for the first to third cycles [53]. Voltage difference of redox peak at 3.67 V during the first discharge–charge cycle shows the biggest distinguish with 0.171 V, 0.165 V, 0.151V for CN8-1, CN8-2 and CN8-3 respectively, thus leading to a higher reversible specific capacity for CN8-3.

The specific capacities of CN5-3 is better than that of CN5-1 and CN5-2, and the specific discharge capacity of CN5-3 is around 170.09 mAh g^{-1}, whereas those of CN5-2 and CN5-1 are about 165.64 and 158.43 mAh g^{-1}, respectively. The specific capacities of CN6-3 and CN8-3 are similar higher than other disordered samples. Higher Li^+/Ni^{2+} disorder is responsible for the lower initial discharge capacity of CN5-1, CN6-1 and CN8-1 samples, which leads to more occupation of Li^+ position by Ni^{2+} ions and hinders the migration of Li^+. Figure 7df show the comparative rate performances at different current densities of 0.1, 0.2, 0.5, 1, 2, and 3 C between 3.0 and 4.3 V, respectively. The rate performances of CN5-3, CN6-3 and CN8-3 samples are markedly enhanced compared with those of other samples. The poor rate performances of CN5-1, CN6-1 and CN8-1 are attributed to the existence of more crystal interface between the initial particles, which results in internal stress due to the de-intercalation of Li^+ during charge and discharge, especially at high current density, microcracks inside the particles and increasing occurrence of side effects. However, the well orientated internal structures afford efficient ion transport for fast Li^+ transport kinetics, further confirming the unique advantages of the cathode materials corresponding to the highly ordered intercalated precursor structure [54-57]. Moreover, the

cycling performances and coulombic efficiency were demonstrated in Figure 7gi at 1 C. The CN5-3 presents an excellent long-term cycling stability, retaining about 88.9% of the initial capacity after 100 cycles. On the other hand, with the increase of nickel content, the cycle performance of high nickel materials is greatly improved due to the increase of order degree. It is mainly because directional arrangement crystal cathodes can alleviate the side reaction and stabilize the crystal structure, and the faster Li^+ transport helps to alleviate the increasing polarization during cycling.

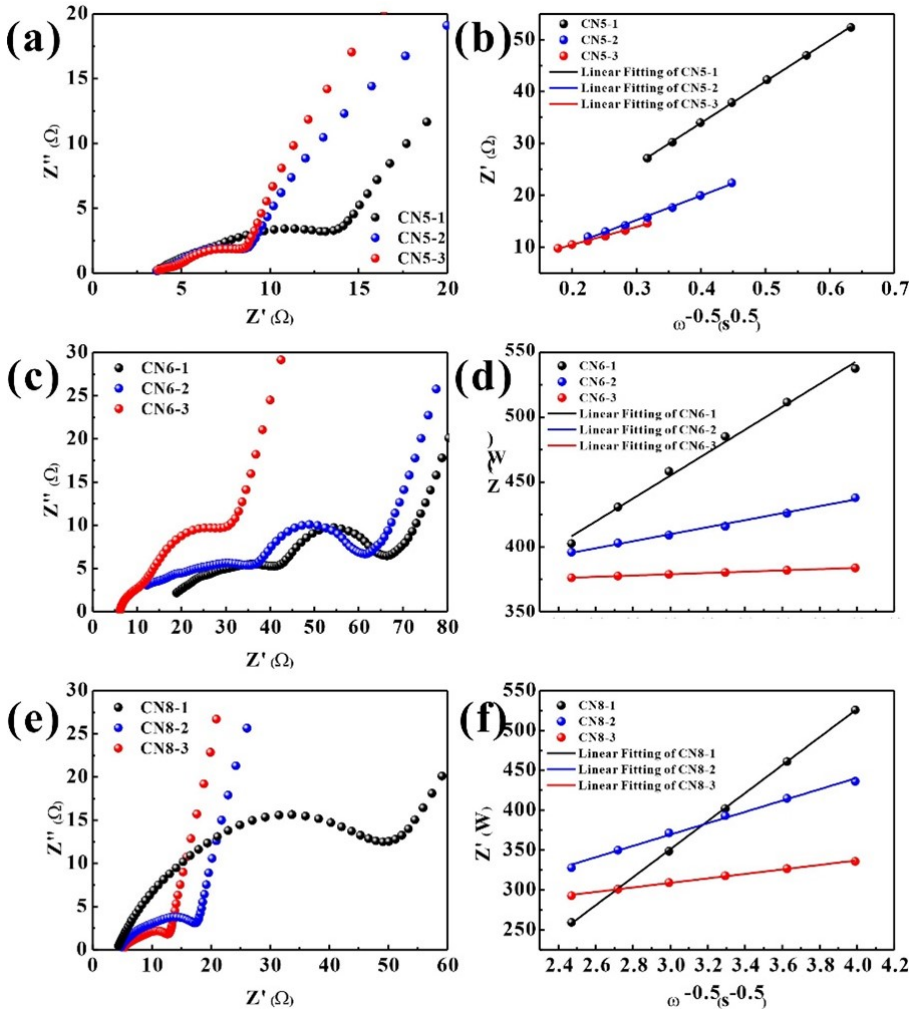

Figure 9: Electrochemical performances (a) Nyquist plots of the three samples, (b) Correlation curve between Z' and $\omega^{-0.5}$.

To support this conclusion, the EIS measurement was employed to analyze the kinetic processes of the Li ion migration in electrodes. The Nyquist diagrams of samples after 100 cycles are presented in Fig. 9a, c, and e. There are two semicircles and a straight line in the EIS, the first semicircle in the high frequency region refers to the resistance of solid electrolyte interphase film (*Rsf*), and the second semicircle at an intermediate frequency corresponds to charge-transfer resistance (*Rct*). The slope represents the Li-ion diffusion in bulk materials [58]. the *Rct* values of CN1, CN2 and CN3 decrease from 14.41 Ω, 6.95 Ω to 6.54 Ω, the *Rct* of CN6-3 (34.82 Ω) is lower than CN6-1 (47.28 Ω), and the *Rct* of CN8-3 (8.841 Ω) is significantly lower than CN8-1 (56.09 Ω) and CN8-2 (15.93 Ω). The results show that the second semicircle of ordered samples is smaller than that of disordered samples after cycling, suggesting that the well orientated internal structures can decrease the charge-transfer. The higher the nickel content, the greater the influence of precursor morphology on the impedance of cathode materials. To further measure the D_{Li+} and the Li-ion diffusion rate, the Li ion diffusion coefficient (D_{Li}) is then calculated by the following equation [47]

$$D_{Li+} = \left(\frac{RT}{\sqrt{2}An^2F^2\sigma C}\right)2$$

where *R*, *T*, *n*, *F*, *A, C* and *σ* represent the gas constant, absolute temperature, number of electrons per molecule involved in the electrochemical reaction, Faraday constant, active electrochemical reaction area, concentration of lithium ions in materials and Warburg factor, respectively, which can be obtained from the slope of the lines in Fig. 9b, d, and f. The CN6-1, CN6-2, CN8-1 and CN8-2 have a higher activation energy barrier for lithium diffusion and the lithium diffusivity was much lower, which are 5.19×10^{-12}, 8.34×10^{-12}, 7.68×10^{-10} cm^2 s^{-1} for the ordered structure of CN5-3, CN6-3 and CN8-3 materials, respectively. The results show that the highly ordered intercalation structure makes Li^+ have a lower diffusion resistance, thus improving the electrochemical performance of the material. With the increase of nickel content, the influence of precursor shape and structure on the impedance of cathode material is greater [26].

Conclusion

In summary, this paper systematically studies the internal structure characteristics of precursors with different nickel contents, and further explores its influence on the electrochemical performance of cathode materials. We found that by adjusting the pH values and the ammonia concentrations, the primary particles are gradually well-directional and orderly stacked or interlaced along the direction of the [001] crystal axis, and with the increase of nickel content, the precursor changes from nanosheets to nanoneedles. These morphological distributions are inherited, which promotes the growth of the cathode material along the [003] direction. The directionally ordered cathode materials have good layered structure and low Li^+/Ni^{2+} mixing, which afford efficient ion transport for fast Li^+ transport kinetics and lead to superior rate capability and good cycle stability. With the increase of nickel content, the morphology distribution of the precursor has a more significant effect on the electrochemical properties of the cathode materials. Our research offers a novel strategy and facile approach for producing the high-performance cathode materials.

Acknowledgements

This work was financiallsy supported by the General Project of Beijing Natural Science Foundation (2222030), the Key R&D Projects in Gansu Province (22YF7GD193).

References

1. PY Hou, HZ Zhang, ZY Zi, LQ Zhang, XJ Xu (2017) Core–shell and concentration-gradient cathodes prepared via co-precipitation reaction for advanced lithium-ion batteries. Journal of Materials Chemistry A 5: 4254-79.

2. PP Pang, XX Tan, Z Wang, ZJ Cai, JM Nan, ZY Xing, H Li (2021) Crack-free single-crystal LiNi0.83Co0.10Mn0.07O2 as cycling/thermal stable cathode materials for high-voltage lithium-ion batteries. Electrochimica Acta 365: 137380-9.

3. N Nitta1, FX Wu, JT Lee, YS Gleb (2015) Li-ion battery materials: present and future. Mater 18: 252-64.

4. ST Myung, FL Maglia, KJ Park, CS Yoon, P Lamp, et al., (2017) Nickel-rich layered cathode materials for automotive lithium-ion batteries: achievements and perspectives, ACS Energy Lett 2 :196-23.

5. HJ Yu, YM Qian, M Otani, DM Tang, SH Guo, et al., (2014) Study of the lithium/nickel ions exchange in the layered LiNi0.42Mn0.42Co0.16O2 cathode material for lithium-ion batteries: experimental and first-principles calculations. Energy & Environmental Science, 7:1068-78

6. F Schipper, EM Erickson, C Erk, JY Shin, FF Chesneau, et al., (2016) Review—Recent Advances and Remaining Challenges for Lithium-Ion Battery Cathodes. Journal of The Electrochemical Society, 164: A6220-8.

7. CH Wang, RZ Yu, S Hwang, JW Liang, XN Li, et al., (2020) Single crystal cathodes enabling high-performance all-solid-state lithium-ion batteries. Energy Storage Materials, 30: 98-103.

8. T Ohzuku, Y Makimura. (2001) Layered lithium insertion material of LiCo1/3Ni1/3Mn1/ 3O2 for lithium-ion batteries, Chem. Lett. 30: 642-3.

9. J Li, HY Li, W Stone, R Weber, S Hy, et al., (2017) Synthesis of single crystal LiNi0.5Mn0.3Co0.2O2 for lithium-ion batteries, 164: A3529-37.

10. HY Li, J Li, XW Ma, JR Dahn (2018) Synthesis of single crystal LiNi0.6Mn0.2Co0.2O2 with enhanced electrochemical performance for lithium-ion batteries, 165: A1038-45.

11. X Zhang, GR Hu, ZD Peng, YB Cao, LY Li, et al., (2021) Synthesis and characterization of mono-dispersion LiNi0.8Co0.1Mn0.1O2 micrometer particles for lithium-ion batteries, Ceram. Int. 47: 25680-8.

12. ZJ Huang, ZX Wang, Q Jing, HJ Guo, XH Li, et al., (2016) Investigation on the effect of Na doping on structure and Li-ion kinetics of layered LiNi0.6Co0.2Mn0.2O2 cathode material. Electrochim. Acta 192: 120-6.

13. HJ Yu, YM Qian, M Otani, DM Tang, SH Guo, et al., (2014) Study of the lithium/nickel ions exchange in the layered LiNi0.42Mn0.42Co0.16O2 cathode material for lithium-ion batteries: experimental and first-principles calculations. Energy Environ. Sci. 3: 1068-78.

14. F Lin, IM Markus, D Nordlund, TC Weng, MD Asta, et al., (2014) Surface reconstruction and chemical evolution of stoichiometric layered cathode materials for lithium-ion batteries. Nat Commun, 5: 3529-36.

15. Y Cho, P Oh (2013) A new type of protective surface layer for high-capacity Ni-based cathode materials: nanoscaled surface pillaring layer. Nano Lett, 13: 1145-52.

16. XB Kong, YG Zhang, SY Peng, J Zeng, JB Zhao (2020) Superiority of Single-Crystal to Polycrystalline LiNixCoyMn1–x–yO2

Cathode Materials in Storage Behaviors for Lithium-Ion Batteries. ACS Sustainable Chemistry & Engineering, 8: 14938-48.

17. J Kang, HQ Pham, DH Kang, HY Park, SW Song (2016) Improved rate capability of highly loaded carbon fiber-interwoven LiNi0.6Co0.2Mn0.2O2 cathode material for high-power Li-ion batteries.J. Alloys Compd 657: 464-71.

18. A Manthiram, Bh Song, WD Li (2017) A perspective on nickel-rich layered oxide cathodes for lithium-ion batteries, Energy Storage Materials, 6: 125-39 .

19. B Han, B Key, SH Lapidus, JC Garcia, H Iddir, et al., (2017) Dogan. From Coating to Dopant: How the Transition Metal Composition Affects Alumina Coat- ings on Ni-Rich Cathodes, ACS Appl. Mater. Interfaces, 9: 41291-302.

20. HH Sun, A Manthiram (2017) Impact of Microcrack Generation and Surface Degradation on a Nickel-Rich Layered Li [Ni0.9-Co0.05Mn0.05] O2 Cathode for Lithium-Ion Batteries. Chemistry of Materials, 29: 8486-93.

21. H Gao, JY Cai, GL Xu, LX Li, Y Ren, et al., (2019) Surface modification for suppressing interfacial parasitic reactions of a Nickel-Rich Lithium-ion cathode. Chemistry of Materials: 31: 2723-30.

22. F Lin, MM Isaac, Markus, D Nordlund, TC Weng, et al., (2014) Doeff. Surface reconstruction and chemical evolution of stoichiometric layered cathode materials for lithium-ion batteries. Nat Commun, 5: l-9.

23. J Lee, A Urban, X Li, D Su, G Hautier, et al., (2014) Unlocking the potential of cation-disordered oxides for rechargeable lithium batteries. Scienc: 343: 519-22.

24. K Edström, T Gustafsson, JO Thomas (2004) The cathode-electrolyte interface in the Li-ion battery, Electrochimica Acta, 50: 397-403.

25. AM Andersson, DP Abraham, R Haasch, S MacLaren, J Liu, et al., (2002) Surface characterization of electrodes from high power lithium-ion batteries. Journal of The Electrochemical Society, 149: A1358-69.

26. CK Yang, LY Qi, ZC Zuo, RN Wang, Y Meng, et al., (2016) Insights into the inner structure of high-nickel agglomerate as high--performance lithium-ion cathodes. Journal of Power Sources, 331: 487-94.

27. WN Wang, DC Meng, GN Qian, SJ Xie, YB Shen, et al., (2020) Controlling Particle Size and Phase Purity of “Single-Crystal” LiNi0.5Mn1.5O4 in Molten-Salt-Assisted Synthesis. The Journal of Physical Chemistry C, 124: 27937-45.

28. J Zhu, JC Zheng, GL Cao, YJ Li, Y Zhou, et al., (2020) Flux-free synthesis of single-crystal LiNi0.8Co0.1Mn0.1O2 boosts its electrochemical performance in lithium batteries. Journal of Power Sources, 464: 1-11

29. YZ Wang, E Wang, X Zhang, X Zhang. HJ Yu (2021) High-Voltage “Single-Crystal” Cathode Materials for Lithium-Ion Batteries. Energy & Fuels, 35: 1918-32.

30. XD Tang, QK Guo, MM Zhou, SW Zhong (2021) Direct regeneration of LiNi0.5Co0.2Mn0.3O2 cathode material from spent lithium-ion batteries. Chinese Journal of Chemical Engineering, 40: 278-86.

31. K Du, FJ Zhu, Q Sun, et al., (2021) Ni0.6Co0.2Mn0.2(OH)2 with dispersed hexagonal slabs enables synthesis of single crystal LiNi0.6Co0.2Mn0.2O2 with enhanced electrochemical performance for lithium-ion batteries.Journal of Alloys and Compounds, 873: 159839-50.

32. SY Yin, WT Deng, J Chen, X Gao, GQ Zou, et al., (2021) Fundamental and solutions of microcrack in Ni-rich layered oxide

cathode materials of lithium-ion batteries. Nano Energy, 83: 105854-86.

33. Y Yang, SM Xu, M Xie, YH He, GY Huang, et al., (2015) Growth mechanisms for spherical mixed hydroxide agglomerates prepared by co-precipitation method: A case of Ni1/3Co1/3Mn1/3(OH)2. Journal of Alloys and Compounds, 619: 846-53.

34. FQ Cheng, YL Xin, JT Chen, L Lu, XX Zhang, et al., (2013) Monodisperse Li1.2Mn0.6Ni0.2O2 microspheres with enhanced lithium storage capability. 1: 5301-08.

35. X Yang,YJ Zhang, J Xiao, YY Zhang, P Dong, Q Meng, et al., (2021) Restoring Surface Defect Crystal of Li-Lacking LiNi0.6-Co0.2Mn0.2O2 Material Particles toward More Efficient Recycling of Lithium-Ion Batteries. ACS Sustainable Chemistry & Engineering, 9: 16997-17006.

36. W Liu, JX Li, WT Li, HY Xu, C Zhang, et al., (2020) Inhibition of transition metals dissolution in cobalt-free cathode with ultrathin robust interphase in concentrated electrolyte. Nat. Commun, 11: 1-11.

37. J Zeng, YH Cui, DY Qu, Q Zhang, JW Wu, et al., (2016) Zhang. Facile synthesis of platelike hierarchical Li1.2Mn0.54Ni0.13-Co0.13O2 with exposed {010} planes for high-rate and long cycling-stable lithium ion batteries. ACS Appl. Mater. Interfaces, 8: 26082-90.

38. YF Su, G Chen, L Chen (2018) Exposing the {010} Planes by Oriented Self-Assembly with Nanosheets To Improve the Electrochemical Performances of Ni-Rich Li[Ni0.8Co0.1Mn0.1]O2 Microspheres. ACS Appl. Mater. Interfaces 10: 6407-14.

39. XH Yang, ZC Zuo, HY Wang, QB Chen, H Zhang, et al., (2015) The Contradiction Between the Half-Cell and Full-Battery Evaluations on the Tungsten-Coating LiNi0.5Co0.2Mn0.3O2 Cathode. Electrochimica Acta, 180: 604-9.

40. NS Choi, ZH Chen, SA Freunberger, XL Ji, YK Sun, et al., (2012) Challenges facing lithium batteries and electrical double-layer capacitors. Angew Chem Int Ed Engl, 51: 9994-10024.

41. QQ Zhang, K Liu, C Li, L Li, XJ Liu, et al., (2021) Zhang. In Situ Induced Surface Reconstruction of Single-Crystal Lithium-Ion Cathode Toward Effective Interface Compatibility. ACS Appl Mater Interfaces, 13: 13771-80.

42. AE Abdel-Ghany, AM Hashem, EA Elzahany, HA Abuzeid, S Indris, et al., (2016) Structural properties and application in lithium cells of Li(Ni0.5Co0.5)1FeO2 ($0 \leq y \leq 0.25$) prepared by sol–gel route: Doping optimization. Journal of Power Sources, 320: 168-179.

43. ZY Wang, Y Zhang, BJ Chen, C Lu (2014) Study on decrystallization of cathode material and decomposition of electrolyte in LiNi1/3Co1/3Mn1/3O2-based cells. Journal of Solid State Electrochemistry, 18: 1757-62.

44. J Langdon, A Manthiram (2021) A perspective on single-crystal layered oxide cathodes for lithium-ion batteries. Energy Storage Materials, 37: 143-60.

45. H Peng, SX Zhao, C Huang, LQ Yu, ZQ Fang, et al., (2020) In Situ Construction of Spinel Coating on the Surface of a Lithium-Rich Manganese-Based Single Crystal for Inhibiting Voltage Fade. ACS Appl Mater Interfaces, 12: 11579-88.

46. HL Zhang, ZH Li, SS Yu, QZ Xiao, GT Lei, et al., (2016) Carbon-encapsulated LiMn2O4 spheres prepared using a polymer microgel reactor for high-power lithium-ion batteries. Journal of Power Sources, 301: 376-85.

47. HL Zhang, ZH Li, SS Yu, QZ Xiao, GT Lei, et al., (2018) Capacity Fading of Ni-Rich Li[NixCoyMn1−x−y]O2 ($0.6 \leq x \leq 0.95$) Cathodes for High-Energy-Density Lithium-Ion Batteries: Bulk or Surface Degradation? Chemistry of Materials, 30: 1155-63.

48. K Du, FJ Zhu, Q Sun, GR Hu, ZD Peng, et al., (2021) Ni0.6Co0.2Mn0.2(OH)2 with dispersed hexagonal slabs enables synthesis of single crystal LiNi0.6Co0.2Mn0.2O2 with enhanced electrochemical performance for lithium-ion batteries. Journal of Alloys and Compounds, 873: 159839-48.

49. M Sale, M Avdeev (2012) 3DBVSMAPPER: a program for automatically generating bond-valence sum landscapes. Journal of Applied Crystallography, 45: 1054-6.

50. K Chiba, A Yoshizawa, Y Isogai (2020) Thermal safety diagram for lithium-ion battery using single-crystal and polycrystalline particles LiNi0.8Co0.1Mn0.1O2. Journal of Energy Storage, 32: 101775-82

51. H Cha, J Kim, H Lee, N Kim, J Hwang, et al., (2020) Boosting Reaction Homogeneity in High-Energy Lithium-Ion Battery Cathode Materials. Adv Mater, 32: 2003040-50.

52. Z Zhang, FY Liu, ZY Huang, MY Yi, XM Fan, et al., (2022) Improving interfacial stability of ultrahigh-voltage lithium metal batteries with single-crystal Ni-rich cathode via a multifunctional additive strategy 608: 1471-80.

53. J Liu, Z Du, X Wang, S Tan, X Wu, et al., (2021) Anionic redox induced anomalousstructural transition in Ni-rich cathodes. Energy Environ. Sci, 14: 6441-54.

54. N Zhao, J Chen, ZQ Liu, KJ Ban, WJ Duan (2018) Porous LiNi1/3Co1/3Mn1/3O2 microsheets assembled with single crystal nanoparticles as cathode materials for lithium ion batteries. Journal of Alloys and Compounds, 768: 782-8.

55. ZY Zhao, B Huang, M Wang, XW Yang, YJ Gu, (2019) Facile synthesis of fluorine doped single crystal Ni-rich cathode material for lithium-ion batteries. Solid State Ionics, 342: 115065-4.

56. X Ji, HJ Li, ZG Wu, S Cheng, HR Hu (2011) Growth of AlN hexagonal oriented complex nanostructures induced by nucleus arrangement. CrystEngComm, 13: 5198-203

57. C Liu, MM Wu, YH Zong, L Zhang, Y Yang et al., (2019) Synthesis and structural properties of xLi2MnO3⋅(1-x) LiNi0.5Mn0.5O2 single crystals towards enhancing reversibility for lithium-ion battery/pouch cells. Journal of Alloys and Compounds, 770: 490-9.

58. M Wang, M Luo, YB Chen, YF Su, L Chen, et al., (2017) Electrochemical deintercalation kinetics of 0.5Li2MnO3·0.5LiNi1/3Mn1/3Co1/3O2 studied by EIS and PITT, J. Alloy. Compd. 696: 907-13.

Submit your next manuscript to Annex Publishers and benefit from:

- Easy online submission process
- Rapid peer review process
- Online article availability soon after acceptance for Publication
- Open access: articles available free online
- More accessibility of the articles to the readers/researchers within the field
- Better discount on subsequent article submission

Submit your manuscript at
http://www.annexpublishers.com/paper-submission.php